The Cryosphere Discuss., 5, 779–809, 2011
www.the-cryosphere-discuss.net/5/779/2011/
doi:10.5194/tcd-5-779-2011

The Cryosphere Discussions

The seasonal cycle and interannual variability of surface energy balance and melt in the ablation zone of the west Greenland ice sheet

M. van den Broeke, R. van de Wal, and P. Smeets

Institute for Marine and Atmospheric research (IMAU), Utrecht University, the Netherlands

Received: 18 February 2011 – Accepted: 23 February 2011 – Published: 7 March 2011

Correspondence to: M. van den Broeke (m.r.vandenbroeke@uu.nl)

Published by Copernicus Publications on behalf of the European Geosciences Union.

Abstract

We present the seasonal cycle and interannual variability of the surface energy balance (SEB) in the ablation zone of the west Greenland ice sheet, using seven years (September 2003–August 2010) of hourly observations from three automatic weather stations (AWS). The AWS are situated along the 67° N latitude circle at elevations of 490 m a.s.l. (S5), 1020 m a.s.l. (S6) and 1520 m a.s.l. (S9) at distances of 6, 38 and 88 km from the ice sheet margin. The hourly AWS data are fed into a model that calculates all SEB components and melt rate; the model allows for shortwave radiation penetration in ice and time-varying surface momentum roughness. Snow depth is prescribed from albedo and sonic height ranger observations. Modelled and observed surface temperatures for non-melting conditions agree very well, with RMSE's of 0.97–1.26 K. Modelled and observed ice melt rates at the two lowest sites also show very good agreement, both for total cumulative and 10-day cumulated amounts. Melt frequencies and melt rates at the AWS sites are discussed. Although absorbed shortwave radiation is the most important energy source for melt at all three sites, interannual melt variability at the lowest site is driven mainly by variability in the turbulent flux of sensible heat. This is explained by the quasi-constant summer albedo in the lower ablation zone, limiting the influence of the melt-albedo feedback, and the proximity of the snow free tundra, which heats up considerably in summer.

1 Introduction

Surface melt and subsequent runoff of meltwater are of primary importance for the mass balance of the Greenland ice sheet (GrIS). Strong interactions exist between surface meltwater production and the sliding behaviour of the ice sheet in west Greenland (Zwally and others, 2005; Van de Wal and others, 2008; Joughin and others, 2008; Shepherd and others, 2009), a process that is linked to the formation and decay of subglacial meltwater channels (Schoof, 2010). The increase in runoff since 1990, following

TCD
5, 779–809, 2011

atmospheric warming (Box and Cohen, 2006; Hanna and others, 2008), explains more than half of the recent mass loss of the GrIS (Van den Broeke and others, 2009). In the warm summers of 2007 and 2010 (Tedesco and others, 2008; 2011), melting on the GrIS exceeded 600 Gt yr^{-1}, an increase of >60% compared to the 1961–1990 average. Especially in areas where the ice sheet borders on tundra, which heats up considerably in summer, summer melt rates can attain 4–5 m of ice (Van de Wal and others, 2005). If in a future warmer climate the ice sheet further retreats onto the land, surface meltwater runoff will continue to dominate GrIS mass loss, making it a crucial parameter to model correctly.

In the absence of detailed observations, estimating melt and runoff from the GrIS requires the use of a regional atmospheric model that solves the full surface energy balance (SEB) at high spatial resolution (Fettweis, 2007; Ettema and others, 2009; Fettweis and others, 2010). In turn, these models require validation from in situ observations at the ice sheet surface (Ettema and others, 2010a, b). Owing to the difficult terrain in the GrIS ablation zone with crevasses, slush formation and the presence of meltwater lakes (Box and Ski, 2007), only a few SEB time series are available to date (Ambach, 1977; Greuell and Konzelmann, 1994; Oerlemans and Vugts, 1993; Henneken and others, 1994; Van de Wal and Russell, 1994; Bøggild and others, 1994; Konzelmann and Braithwaite, 1995; Heinemann 1999). Most experiments lasted only for (part of) a single ablation season, neither capturing the wintertime climate nor the interannual variability.

Automatic weather stations (AWS) may fill these observational gaps in time and space. Since September 2003, the Institute for Marine and Atmospheric Research of Utrecht University (UU/IMAU) operates three AWS in the ablation zone in west Greenland, as a contribution to the Greenland Climate Network (GC-Net, Steffen and Box, 2001). The AWS are equipped with radiation sensors and two measurement levels for temperature, humidity and wind speed, which makes them especially suitable for SEB studies. Previously, the first four years of AWS data (2003–2007) were used to assess the radiation and turbulent driven heat exchange (Van den Broeke, 2008a, 2009b) and

TCD
5, 779–809, 2011

the surface mass balance (Van den Broeke and others, 2008b). This study presents an update, using the longer time series to present the average seasonal cycle of the full energy balance with special reference to interannual variability, including a thorough evaluation of the model under melting and non-melting conditions. The next section describes the AWS data and the SEB model, Sect. 3 presents the model evaluation and the SEB results, followed by a summary and conclusions in Sect. 4.

2 Methods

2.1 AWS data

The three AWS are situated along the K-transect, a stake array in southwest Greenland that extends from the ice margin to 1850 m a.s.l. This part of the GrIS is characterized by a dry and sunny climate, resulting in little wintertime accumulation (Van den Broeke and others, 2008b) and high summertime ablation rates of up to 5 m near the ice margin (Van de Wal and others, 2005). The AWS masts are not fixed to the ice and sink with the ablating surface, while approximately retaining their upright position. Each site is equipped with an independent sonic height ranger, fixed to the ice, to monitor snow accumulation and snow/ice ablation, as well as one or several aluminium stakes to measure annual net ablation/accumulation at the end of the ablation season. Figure 1 shows the location and surroundings of the three AWS sites S5 (490 m a.s.l.), S6 (1020 m a.s.l.) and S9 (1520 m a.s.l.) superimposed on a MODIS image from 23 August 2006. This time of year marks the end of the ablation season, when the bare ice extent is at a maximum; clearly visible are the bare ice zone (greyish, between 500–1500 m asl), the superimposed ice zone (milky blue, 1500–1750 m a.s.l.) and the snow-covered percolation zone (bright white, 1750 m a.s.l. and higher). Melting of dust-rich glacier ice causes the dark band in the middle ablation zone (Wientjes and Oerlemans, 2010). Strong interactions between surface meltwater production and ice dynamics have been observed along the K-transect (Van de Wal and others, 2008; Shepherd and others, 2009).

TCD
5, 779–809, 2011

Half-hourly averages of air pressure, shortwave/longwave incoming/outgoing radiation components and two-level wind speed/direction, temperature and relative humidity are stored at the AWS and retrieved each year in August or September. Table 1 lists the sensor specifications and Table 2 the period of operation, location information and basic climate and surface energy balance statistics. Radiation, temperature and humidity observations are corrected along the lines described in Van den Broeke and others (2004, 2008a). Owing to a datalogger failure, S6 misses data from September 2007 to August 2008, and for several weeks in June, July and August 2010. This prevented the calculation of averages for those months at S6.

The SEB model requires time series of snow depth, instrument height and surface momentum roughness z_0. The first step is to determine whether ice or snow is present at the surface; for this, a combination of albedo ($SW_{in}/|SW_{out}|$) and surface height measurements is used. As an example, Fig. 2 shows the evolution of albedo (blue line), surface level from the sonic height ranger (orange line), the deduced ice horizon (red line) and derived snow depth (green line) at S6 for the summer of 2004. After the thin layer (25 cm) of winter snow has melted, background albedo gradually decreases in the course of the melt season. This slow evolution is caused by snow metamorphism under the influence of melt and the fact that the radiation sensor, mounted at approximately 6 m above the surface, "sees" a much larger surface area (approximately 100 m^2) than the sonic height ranger, which is located closer to the surface and has a smaller viewing angle. Even when the snow may have disappeared under the sonic height ranger, the radiation sensor still detects patches of snow, usually in gullies, keeping the albedo well above 0.6. Only after these patches have completely melted away towards the end of the ablation season, does the albedo reach the value of glacier ice (approximately 0.55). Superimposed on this gradual background decrease in albedo are rapid fluctuations. These are caused by summer snowfall events, and in spite of their small magnitude (typically <5 cm) are important because they temporarily reduce or even halt surface ice melt. The combination of albedo and sonic height ranger data is used to derive snow depth at S5 and S6 for the full observational period.

TCD
5, 779–809, 2011

Albedo measurements at S9 suggest that glacier ice did not surface there (supported by ground observations), and a semi-infinite snowpack is prescribed for that site. Instrument levels (heights above the surface) are reconstructed based on the derived snow depths and reference measurements during annual station visits. In combination with the two-level wind speed, temperature and humidity data this information is used to calculate 20-day running means of surface momentum roughness z_0 (Van den Broeke and others, 2009b).

2.2 SEB model

The SEB of a "skin" layer is given by:

$$\begin{aligned} M &= SW_{in} + SW_{out} + LW_{in} + LW_{out} + SHF + LHF + G_s \\ &= SW_{net} + LW_{net} + SHF + LHF + G_s [Wm^{-2}] \\ &= R_{net} + SHF + LHF + G_s \end{aligned} \quad (1)$$

where M is melt energy, SW_{in}, SW_{out} and SW_{net} are incoming, reflected and net shortwave radiation fluxes, LW_{in}, LW_{out} and LW_{net} are incoming, emitted and net longwave radiation fluxes, R_{net} is the net radiation flux, SHF and LHF are the turbulent fluxes of sensible and latent heat and G_s is the subsurface (conductive) heat flux, evaluated at the surface. All terms are defined positive when directed towards the surface. As input the SEB model uses hourly values of z_0, (corrected) single-level measurements of wind speed, temperature and humidity, SW_{in}, SW_{out} and LW_{in}. The scalar roughness lengths for heat (z_h) and moisture (z_q) are calculated using the expressions of Andreas (1987), including the adjustments for very rough ice surfaces proposed by Smeets and Van den Broeke (2008b).

The SEB model solves Eq. (1) to obtain surface temperature T_s, using bisection and nested iterative procedures for the stability corrections in the turbulent heat flux calculations, assuming the surface to be saturated with respect to ice (or water when the surface is melting). If T_s exceeds the melting point, it is reset to 273.15 K and all remaining energy is used for melt. This way of working assumes a closed energy balance

TCD
5, 779–809, 2011

and therewith differs from Van den Broeke (2008a, 2009b), who did not require melt rate to be quantified and therefore could use "observed" T_s (from LW_{out}) to calculate the radiation balance and turbulent fluxes.

Equation (1) assumes all energy to be absorbed at the surface, neglecting penetration of shortwave radiation to levels below the surface. This may be justified for fine-grained dry snow, but not for bare glacier ice. When ice is exposed at the surface at S5 and S6, the model of Brandt and Warren (1993) is used to calculate the subsurface shortwave radiation flux. This model is based on Mie scattering in a medium of perfectly stacked spherical particles with 2.5 mm diameter combined with the two-stream approach of Schlatter (1972), using 118 wavelength bands to account for the highly wavelength-dependent absorption properties of ice. We correct the incoming shortwave spectrum for atmospheric mass and the presence of clouds, the latter parameterized using the expressions of Kuipers Munneke and others (2010). The radiation grid has 1 mm resolution to a depth of 5 m, after which radiative heating is interpolated to the coarser temperature grid.

3 Results

3.1 Model evaluation for melting and non-melting conditions

The modelled SEB must be evaluated separately for melting and non-melting conditions. When the surface is not melting, modelled values of surface temperature T_s can be compared to "observed" values derived from LW_{out}. Assuming a constant, unit longwave emissivity of the snow/ice surface, the results for observed and modelled hourly and monthly mean T_s are presented in Fig. 3a–c. The model performs well, with an average difference for hourly values between −0.28 K at S5 and 0.34 K at S9. The RMSE decreases from 1.26 K at S5 to 0.97 K at S9. The better performance of the model in the higher ablation zone is probably associated with the smaller summer ablation, resulting in smaller mast displacement and tilt, and hence smaller corrections for the shortwave radiation measurements.

TCD
5, 779–809, 2011

During melt conditions, T_s is constant and therefore not a useful variable to evaluate the SEB model. Instead we compare observed and modelled melt rates for ice, which has a well-known density (910 kg m^{-3}), thus enabling a conversion from height change (as measured by the sonic height ranger) to mass change and hence (modelled) melt energy. This does not work for S9, where the surface consists of snow/firn with unknown density, but it works well for S5 and S6, where ice is frequently present at the surface and can easily be detected (Fig. 2). Figure 4a shows that cumulative ice melt measured by the sonic height rangers at S5 (26.9×10^3 kg m^{-2}) and S6 (10.5×10^3 kg m^{-2}) is matched by the SEB model to within 1.9% (S5) and 1.6% (S6). The difference between the sonic height ranger and the ablation stake measurements (triangles in Fig. 4a) is an indication of the observational uncertainty, arising from instrumental error, from the fact hat the observations are not performed at exactly the same location but especially from the fact that stake measurements are not very accurate in the first place. At S5, modelled cumulative ice ablation follows the stake measurements better than the continuous track of the sonic height ranger. At both sites, observed and modelled cumulative melt agree to within the observational uncertainty. A stricter evaluation of the SEB model is to compare observed and modelled ice melt over shorter periods (Fig. 4b). A 10-day period is chosen, to reduce the measurement noise of the sonic height ranger to a level that enables a meaningful comparison. Again, agreement between modelled and observed ice melt is very good at both sites (S5: $r = 0.99$, slope = 0.96, RMSE = 2.1 kg m^{-2} day^{-1}; S6: $r = 0.98$, slope = 0.98, RMSE = 1.7 kg m^{-2} day^{-1}).

We conclude that during melting conditions, the SEB model is capable of reliably simulating interannual and intra-seasonal melt rate variability. During non-melting conditions, the SEB model accurately simulates the surface temperature. These results lend credibility to the modelled SEB components.

TCD
5, 779–809, 2011

3.2 Average seasonal cycle of the SEB

Table 2 shows some climate and energy balance statistics. The lapse rate of 2 m temperature is 7.4 K km^{-1} between S5 and S6 and 5.8 K km^{-1} between S6 and S9. The stronger temperature decrease near the margin reflects the effect of the warm summertime tundra on the temperature at S5. The relative humidity increases towards higher elevation, but specific humidity decreases owing to lower temperatures that limit the atmospheric moisture content. Wind speed becomes significantly larger towards the interior, which is partly caused by the smaller momentum roughness, and partly by the greater influence of the high winds in the Greenland interior (Van Angelen and others, 2011). The thinner atmosphere at S9 transmits more shortwave radiation, but as the average surface albedo is also higher, and the latter effect dominates, net shortwave radiation (SW_{net}) decreases from S5 to S9. As a result of the warm air from the tundra during summer, the flux of sensible heat (SHF) towards the surface is also greatest at S5. The gradients in these two SEB components (SW_{net} and SHF) are the main reason for the exponential increase of melt energy when going from S9 to S5.

Figure 5 displays the average seasonal cycle of monthly melt frequency at the AWS sites. The error bars represent one standard deviation for the monthly means. Annual average modelled melt frequencies are 28% at S5, 16% at S6 and 12% at S9. At S5, melt may occur in any month of the year, even occasionally in mid-winter. In the lower ablation zone the melt season usually starts at the end of April, with an average melt frequency of several %. May marks the start of the ablation season in the middle to higher ablation zone, with melt frequencies of 15% at S6 to 8% at S9. Melt frequency peaks in July at all AWS, and varies from 52% at S9, 68% at S6 and 88% at S5. September is still a significant melt month at S5 and S6, with average melt frequencies of 30 and 10%, respectively.

Figure 6a shows the average seasonal cycle of albedo at the three sites. The error bars represent one standard deviation for the monthly means, and for clarity the seasonal cycle of the standard deviation is plotted separately in Fig. 6b. The shape of the

TCD
5, 779–809, 2011

seasonal cycle at S5 differs significantly from that at S6 and S9. Winter accumulation is small at S5, owing to significant wintertime snowdrift sublimation and the infilling with snow of the abundant crevasses. In late winter and spring, the surface at S5 consists of a mix of bare ice and snow, which explains the intermediate albedo values and very large standard deviations in the period February–April. Persistent melt causes the relatively dark glacier ice to be exposed throughout summer, leading to low albedo values and low interannual variability. At S6, the surface is covered by snow until May, but melt may occur in April and May, resulting in an increase in the standard deviation. June is a transition month. In July and August, ice is exposed at S6 and the albedo reaches its minimum, but summer snowfalls (see Fig. 2) keep the interannual variability high. At S9, melting does not occur until June, when albedo starts to decrease and variability increases. At this site, glacier ice is not exposed, and the seasonal cycle in albedo reflects the progressive metamorphism of the firn under the influence of melt. Interannual variability peaks in July, caused by summer snowfalls.

Figure 7a–c shows the average seasonal cycle of SEB components at the three AWS sites. We have integrated the energy fluxes from the surface to the lowest ice level in the model, so that a single value can be presented for SW_{net}, G and M. The error bars represent one standard deviation for the monthly means. The amplitude of the main forcing component of the seasonal cycle in the SEB, SW_{net}, on average decreases towards higher elevations, a result of the higher average surface albedo. The shape of the seasonal SEB cycle at S5 differs significantly from that at S6 and S9, as a result of the different seasonal cycle of albedo. At S5, SW_{net} is distributed rather symmetrically around the summer solstice, while at S6 and S9, the more gradual decrease of albedo causes the seasonal cycle of SW_{net} to be less symmetric, with a slow increase towards a peak in July and a rapid decrease in fall.

Being situated on the protruding tongue of Russell glacier, the SEB at S5 is influenced by the thermal characteristics of the surrounding ice-free tundra. Especially in July, when most of the moisture has evaporated from the upper tundra layers, 2 m temperatures over the tundra may reach 15–20 °C during sunny conditions (Van den

TCD
5, 779–809, 2011

Broeke and others, 1994). The associated horizontal temperature gradient sets up a pressure perturbation that is favourable for the formation of strong barrier winds that blow from south to north along the large-scale direction of the ice sheet margin (Van den Broeke and Gallée, 1996). This enhances turbulent heat exchange between the ambient atmosphere and the melting ice surface, resulting in significantly positive values of SHF and LHF at S5 (Fig. 7a). SHF shows a double maximum, owing to katabatic wind forcing that prevails in the absence of barrier winds both in summer and winter. The July peaks in SHF and LHF shift the melt peak away from the maximum in SW_{net}. Another effect of the presence of warm tundra air is to enhance LW_{in} through higher ambient temperatures and moisture in the low atmosphere. This results in less negative values of LW_{net}, as LW_{out} is constant under melting conditions. The effect on LW_{net} at S5 is a difference with S6 and S9 of 10–15 $W\,m^{-2}$, representing a significant 10% of the available melt energy at the ice sheet margin.

Higher on the ice sheet at S6 and S9, the temperature and moisture contrasts between ambient atmosphere and (melting) ice surface are less pronounced, resulting in smaller summertime values of SHF, LHF and LW_{net}. At S9, the moisture gradient is reversed and LHF becomes negative and therewith compensates a large part of SHF, a well-known summer phenomenon close to the equilibrium line (Ambach, 1977; Henneken and others, 2004).

3.3 Interannual variability

The good performance of the SEB model and the reasonable length of the time series enables us to use the AWS data for a preliminary study of factors driving interannual melt variability in this part of the GrIS. The error bars in Fig. 5 indicate that interannual variability of midsummer melt frequency increases towards the higher ablation zone. For instance, S9 melt frequencies for June vary from 18% in 2006 to 56% in 2007. The years 2007 and 2010 stand out as high-frequency melt years, with July melt frequency at S9 of almost 70%. In contrast, lower in the ablation zone at S5, the mid-summer melt frequency is remarkably stable from year to year, with July values ranging from

TCD
5, 779–809, 2011

83–93%. Here, the variability is largest in the beginning (May) and end (September) of the ablation season. For instance, September 2003 had a 65% melt frequency at S5, while it was only 18% in 2004 and 2009.

Figure 8a–c shows the time series of monthly mean SEB components at the three AWS sites, including melt frequency (black bars). At S5, the onset and evolution of the ablation season in terms of melt frequency is comparable from year to year. At S6 and S9, there is considerably more interannual variability. For instance, the summers of 2007 and 2010 (until July only) clearly stand out as anomalous, with high melt rates.

Figure 9 shows the cumulative energy sources for melt at the three sites, based on monthly totals and expressed in $GJ\,m^{-2}$. The anomalous melt seasons of 2007 and 2010 stand out especially in the high ablation zone (S9). At all three sites, SW_{net} is the main energy source for melt, followed by SHF. LHF represents a small energy source for melt at S5, is zero at S6 and a small energy sink at S9. The subsurface heat flux is an energy sink at S5 and S6: the impermeable ice does not allow meltwater to refreeze at depth, maintaining the temperature gradient between the upper and lower ice layers; in combination with the large heat conductivity of ice, this efficiently transports heat towards greater depths. At S9, meltwater penetration and refreezing bring the snowpack at the melting point over a considerable depth. In combination with the smaller heat conductivity of snow, this means that G becomes small during melt. At all sites, LW_{net} is the main heat sink during melt.

At S6 and S9, cumulative SW_{net} values exceed total cumulative melt energy. This is possible, because SW_{net} and LW_{net} are themselves highly negatively correlated for monthly totals (Fig. 10). This correlation reflects the fact that clear skies on one hand lead to high monthly totals for SW_{net}, but on the other hand also limit downward atmospheric radiation (LW_{in}), while LW_{out} is constant. The shift in slope at high values of SW_{net} in Fig. 10 is caused by the albedo difference between melting snow (≈0.7) and ice (≈0.55).

Figure 11a summarizes the average contribution of the various SEB components to the melt energy as a function of distance to the ice margin. It confirms that, owing to

TCD
5, 779–809, 2011

the negative correlation of SW_{net} with LW_{net}, the contribution of cumulative R_{net} to melt remains smaller than unity throughout the ablation zone. In the lower ablation zone, the combined contributions of SHF and LHF to melt are similar to R_{net}. In the higher ablation zone, the contributions of SHF and LHF to melt approximately cancel, and R_{net} is the primary energy source for melt. As a heat sink/source for melt, the subsurface heat flux G is generally small.

The fact that SW_{net} (R_{net}) is the main energy source for melt does not necessarily mean that interannual variations in SW_{net} also explain most of the year-to-year variations in melt. To explore this further, we linearly regressed anomalies of monthly cumulative SEB components during melt onto anomalies of monthly cumulative melt energy. Figure 11b shows the slope of the regressions ($\partial\Delta SEB/\partial\Delta M$, where ΔSEB indicates the anomaly of an SEB component from the mean) as a function of distance to the ice margin. The error bars are based on regressions performed on subsets of the data, with a minimum of 0.1. At S6 and S9, $\partial\Delta SW_{net}/\partial\Delta M$ dominates, indicating that interannual variability in SW_{net} explains most of the variability in melt. This is indicative of an active melt-albedo feedback, i.e. the fact that the albedo of melting snow is considerably lower than that of dry snow. At both sites, SHF also explains part of the melt variability, while $\partial\Delta LHF/\partial M$ and $\partial\Delta Gs/\partial M$ are not significantly different from zero.

At S5, $\partial\Delta SHF/\partial\Delta M$ dominates, indicating that changes in SHF are the best predictor for melt variability close to the ice margin. At S5, $\partial\Delta LHF/\partial\Delta M$ is also significant and equally large as $\partial\Delta R_{net}/\partial\Delta M$. This surprising result follows from the fact that the surface at S5 is snow-free for most of the summer. As a result, the surface albedo is more or less constant and the melt-albedo feedback is not active. Moreover, as explained in the previous sections, S5 is under the direct influence of the tundra climate, enhancing the roles of SHF and LHF as energy sources for melt. As the contribution of SHF and LHF to melt is highly variable from year to year, they explain most of the melt variability in spite of the fact that these SEB components contribute less than 50% to the total seasonal melt energy. This is as important as it is interesting, because in

TCD
5, 779–809, 2011

a future warmer climate, when the ice sheet retreats on land and more ice-free land is exposed, the SEB and associated melt climate as presently observed at S5 will become representative for large parts of the marginal ice sheet that are currently adjacent to the ocean.

4 Summary and conclusions

We used seven years of automatic weather station data from the ablation zone in west Greenland to drive a surface energy balance (SEB) model that calculates SEB components, surface temperature and melt rate. Modelled surface temperatures and ice melt rates compare very well to observations. Melt frequency in summer ranges from 80–95% in the lower ablation zone to 35–55% close to the equilibrium line. The average seasonal cycle of melt as well as interannual melt variability is mainly driven by absorption of shortwave radiation; an exception is the lower ablation zone, where the turbulent fluxes of sensible and latent heat contribute significantly to the melt energy, and are also the most important SEB components explaining interannual melt variability. This melt regime, which is typical for ice caps surrounded by ice free land in more temperate climate regions, is expected to become more important in Greenland in a warmer future, when the ice sheet retreats on land. Unfortunately, the AWS observations used in this study are only locally representative and their time series too short to infer trends in the melt regime. An important question therefore remains how representative these observations are for the Greenland ice sheet as a whole, and whether the Greenland melt regime has undergone significant changes in recent decades. This can only be addressed using output of a regional atmospheric climate model (Ettema and others, 2010a, b), and will be explored in a forthcoming study.

Acknowledgements. This work is funded by Utrecht University and the Netherlands Arctic Program (NAP) of the Netherlands Organisation of Scientific Research, section Earth and Life Sciences (NWO/ALW).

TCD
5, 779–809, 2011

References

Ambach, W.: Untersuchungen zum Energieumsatz in der Akkumulationszone des Grönländischen Inlandeises, Meddelelser om Grønland , 187–7, Bianco Lunos Bogtrykkeri A/S, Copenhagen, 1977.

Andreas, E. L.: A theory for the scalar roughness and the scalar transfer coefficients over snow and sea ice, Bound.-Layer Meteorol., 38, 159–184, 1987.

Bøggild, C. E., Reeh, N., and Oerter, H.: Modelling ablation and mass-balance sensitivity to climate change of Storstrømmen, northeast Greenland, Glob. Planet. Change, 9, 79–90, 1994.

Box, J. E. and Cohen, A. E.: Upper-air temperatures around Greenland: 1964–2005, Geophys. Res. Lett., 33, L12706, doi:10.1029/2006GL025723, 2006.

Box, J. E. and Ski, K.: Remote sounding of Greenland supraglacial melt lakes: implications for subglacial hydraulics, J. Glaciol., 53, 257–265, 2007.

Brandt, R. E. and Warren, S. G.: Solar heating rates and temperature profiles in Antarctic snow and ice, J. Glaciol. 39, 99–110, 1993.

Ettema, J., van den Broeke, M. R., van Meijgaard, E., van de Berg, W. J., Bamber, J. L., Box, J. E., and Bales, R. C.: Higher surface mass balance of the Greenland ice sheet revealed by high-resolution climate modeling, Geophys. Res. Lett., 36, L12501, doi:10.1029/2009GL038110, 2009.

Ettema, J., van den Broeke, M. R., van Meijgaard, E., van de Berg, W. J., Box, J. E., and Steffen, K.: Climate of the Greenland ice sheet using a high-resolution climate model – Part 1: Evaluation, Cryosphere, 4, 511–527, 2010.

Ettema, J., van den Broeke, M. R., van Meijgaard, E., and van de Berg, W. J.: Climate of the Greenland ice sheet using a high-resolution climate model – Part 2: Near-surface climate and energy balance, Cryosphere, 4, 529–544, 2010.

Fettweis, X.: Reconstruction of the 1979–2006 Greenland ice sheet surface mass balance using the regional climate model MAR, Cryosphere, 1, 21–40, 2007.

Fettweis, X., Mabille, G., Erpicum, M., Nicolay, S., and van den Broeke, M. R.: The 1958–2009 Greenland ice sheet surface melt and the mid-tropospheric atmospheric circulation, Clim. Dyn., doi:10.1007/s00382-010-0772-8, 2010.

Greuell, W. G. and Konzelmann, T.: Numerical modelling of the energy balance and the englacial temperature of the Greenland Ice Sheet. Calculations for the ETH-Camp location

TCD
5, 779–809, 2011

(West Greenland, 1155 m a.s.l.), Glob. Planet. Change, 9, 91–114, 1994.
Hanna, E., Huybrechts, P., Steffen, K., Cappelen, J., Huff, R., Shuman, C., Irvine-Fynn, T., Wise, S., and Griffiths, M.: Increased Runoff from Melt from the Greenland Ice Sheet: A Response to Global Warming, J. Climate, 21, 331–341, 2008.
Heinemann, G.: The KABEG'97 field experiment: An aircraft-based study of the katabatic wind dynamics over the Greenlandic ice sheet, Bound. Layer Meteorol., 93, 75–116, 1999.
Henneken, E. A. C., Bink, N. J., Vugts, H. F., Cannemeijer, F., and Meesters, A. G. C. A.: A case study of the daily energy balance near the equilibrium line on the Greenland ice sheet, Glob. Planet. Change, 9, 69–78, 1994.
Joughin, I., Das, S. B., King, M. A., Smith, B. E., Howat, I. M., and Moon, T.: Seasonal speedup along the western flank of the Greenland ice sheet, Science, 320, 781–783, 2008.
Konzelmann, T. and Braithwaite, R. J.: Variations of ablation, albedo and energy balance at the margin of the Greenland ice sheet, Kronprins Christian Land, eastern North Greenland., J. Glaciol., 41, 174–182, 1995.
Kuipers Munneke, P., Reijmer, C. H., and van den Broeke, M. R.: Assessing the retrieval of cloud properties from radiation measurements over snow and ice, Int. J. Climatol., doi:10.1002/joc.2114, 2010.
Oerlemans, J. and Vugts, H. F.: A Meteorological Experiment in the Melting Zone of the Greenland Ice Sheet, Bull. Amer. Meteorol. Soc. 74, 355–365, 1993.
Schlatter, T. W.: The local surface energy balance and subsurface temperature regime in Antarctica, J. Appl. Meteorol., 11, 1048–1062, 1972.
Schoof, C.: Ice-sheet acceleration driven by melt supply variability, Nature 468, 803–806, doi:10.1038/nature09618, 2010.
Shepherd, A., Hubbard, A., Nienow, P., King, M., McMillan, M., and Joughin, I.: Greenland ice sheet motion coupled with daily melting in late summer, Geophys. Res. Lett., 36, L01501, doi:10.1029/2008GL035758, 2009.
Smeets, C. J. P. P. and van den Broeke, M. R.: Temporal and spatial variation of momentum roughness length in the ablation zone of the Greenland ice sheet, Bound. Layer Meteorol., 128, 315–338, 2008a.
Smeets, C. J. P. P. and M. R. van den Broeke: The parameterisation of scalar transfer over rough ice surfaces, Bound.-Layer Meteorol., 128, 339–355, 2008b.
Steffen, K. and Box, J. E.: Surface climatology of the Greenland ice sheet: Greenland Climate Network 1995–1999, J. Geophys. Res., 106(D24), 33951–33964, 2001.

TCD
5, 779–809, 2011

Tedesco, M., Fettweis, X., van den Broeke, M. R., van de Wal, R. S. W., and Smeets, P.: Extreme Snowmelt in Northern Greenland During Summer 2008, Eos Trans. AGU, 89, doi:10.1029/2008EO410004, 2008.

Tedesco, M., Fettweis, X., van den Broeke, M. R., van de Wal, R. S. W. Smeets, C. J. P. P., van de Berg, W. J., Serreze, M. C., and, Box, J. E.: The role of albedo and accumulation in the 2010 melting record in Greenland, Environ. Res. Lett., in press, 2011.

Van Angelen, J., van den Broeke, M. R., and van de Berg, W. J.: Momentum budget of the atmospheric boundary layer over the Greenland ice sheet and its surrounding seas, J. Geophys. Res., submitted, 2011.

Van de Wal, R. S. W. and Russell, A., A comparison of energy balance calculations, measured ablation and meltwater runoff near Søndre Strømfjord, West Greenland, Glob. Planet. Change, 9, 29–38, 1994.

Van de Wal, R. S. W., Greuell, W., van den Broeke, M. R., Boot, W., Snellen, H., Reijmer, C. H., and Oerlemans, J.: Mass balance measurements along a transect in West-Greenland over the period 1990–2003, Ann. Glaciol., 42, 311–316, 2005.

Van de Wal, R. S. W., Boot, W., van den Broeke, M. R., Smeets, C. J. P. P., Reijmer, C. H., Donker, J. J. A., and Oerlemans, J.: Large and Rapid Melt-Induced Velocity Changes in the Ablation Zone of the Greenland Ice Sheet, Science, 321, doi:10.1126/science.1158540, 111–113, 2008.

Van den Broeke, M. R., Duynkerke, P. G., and Oerlemans, J.: The observed katabatic flow at the edge of the Greenland ice sheet during GIMEX-91, Glob. Planet. Change, 9, 3–15, 1994.

Van den Broeke, M. R. and Gallée, H.: Observation and simulation of barrier winds at the western margin of the Greenland ice sheet, Q. J. R. Meteorol. Soc., 122, 1365–1383, 1996.

Van den Broeke, M. R., van As, D., Reijmer, C. H., and van de Wal, R. S. W.: Assessing and improving the quality of unattended radiation observations in Antarctica, J. Atmos. Oceanic., 21(9), 1417–1431, 2004.

Van den Broeke, M. R., Smeets, C. J. P. P., Ettema, J., and Kuipers-Munneke, P.: Surface radiation balance in the ablation zone of the west Greenland ice sheet, J. Geophys. Res., 113, D13105, doi:10.1029/2007JD009283, 2008a.

Van den Broeke, M. R., Smeets, C. J. P. P., and Ettema, J., van der Veen, C., van de Wal, R. S. W., and Oerlemans, J.: Partitioning of energy and meltwater fluxes in the ablation zone of the west Greenland ice sheet, Cryosphere, 2, 179–189, 2008b.

TCD
5, 779–809, 2011

Van den Broeke, M. R., Bamber, J., Ettema, J., Rignot, E., Schrama, E., van de Berg, W. J., van Meijgaard, E., Velicogna, I., and Wouters, B.: Partitioning recent Greenland mass loss, Science, 326, 984–986, 2009a.

Van den Broeke, M. R., Smeets, C. J. P. P., and Ettema, J.: Surface layer climate and turbulent exchange in the ablation zone of the west Greenland ice sheet, Int. J. Climatol., doi:10.1002/joc.1815, 2009b.

Wientjes, I. G. M. and Oerlemans, J.: An explanation for the dark region in the western melt zone of the Greenland ice sheet, Cryosphere, 4, 261–268, doi:10.5194/tc-4-261-2010, 2010.

Zwally, H. J., Giovinetto, M. B., Li, J., Cornejo, H. G., Beckley, M. A., Brenner, A. C., Saba, J. L., and Yi, D.: Mass changes of the Greenland and Antarctic ice sheets and shelves and contributions to sea-level rise: 1992–2002, J. Glaciol., 51, 509–527, 2005.

TCD
5, 779–809, 2011

Table 1. AWS sensor specifications. EADT = Estimated Accuracy for Daily Totals.

Sensor	Type	Range	Accuracy
Air pressure	Vaisala PTB101B	600 to 1060 hPa	4 hPa
Air temperature	Vaisala HMP35AC	−80 to + 56 °C	0.3 °C
Relative humidity	Vaisala HMP35AC	0 to 100%	2% (RH < 90%) 3 % (RH > 90%)
Wind speed	Young 05103	0 to 60 m s^{-1}	0.3 m s^{-1}
Wind direction	Young 05103	0 to 360 °	3 °
Pyranometer	Kipp en Zonen CM3	305 to 2800 nm	EADT +/−10%
Pyrradiometer	Kipp en Zonen CG3	5000 to 50 000 nm	EADT+/−10%
Snow height	Campbell SR50	0.5 to 10 m	0.01 m or 0.4%

TCD
5, 779–809, 2011

Table 2. AWS topographic, climate and surface energy balance characteristics.

	S5	S6	S9
Location (August 2006)			
Latitude (N)	67°06′	67°05′	67°03′
Longitude (W)	50°07′	49°23′	48°14′
Elevation (m a.s.l.)	490	1020	1520
Distance from ice edge (km)	6	38	88
Period of operation used for this paper			
Start of observation	1 Sep 2003	1 Sep 2003	1 Sep 2003
End of observation	31 Jul 2010	31 Jul 2010*	31 Jul 2010
Annual average climate variables			
Surface mass balance (m w.e.)	−3.6	−1.5	∼0
2 m temperature (K)	267.2	263.3	260.4
2 m relative humidity (%)	75	87	89
2 m specific humidity (g kg^{-1})	2.3	2.1	1.9
10 m wind speed (m s^{-1})	5.3	6.9	7.9
Annual average surface energy balance variables (W m^{-2})			
SW_{in}	117	131	142
SW_{out}	−73	−94	−110
SW_{net}	45	36	32
LW_{in}	241	227	222
LW_{out}	−280	−269	−260
LW_{net}	−39	−42	−38
R_{net}	6	−6	−6
SHF	38	26	18
LHF	−4	−2	−4
G	2	3	3
M	41	20	11

* September 2007–August 2008, June and July 2010 are missing at S6.

TCD
5, 779–809, 2011

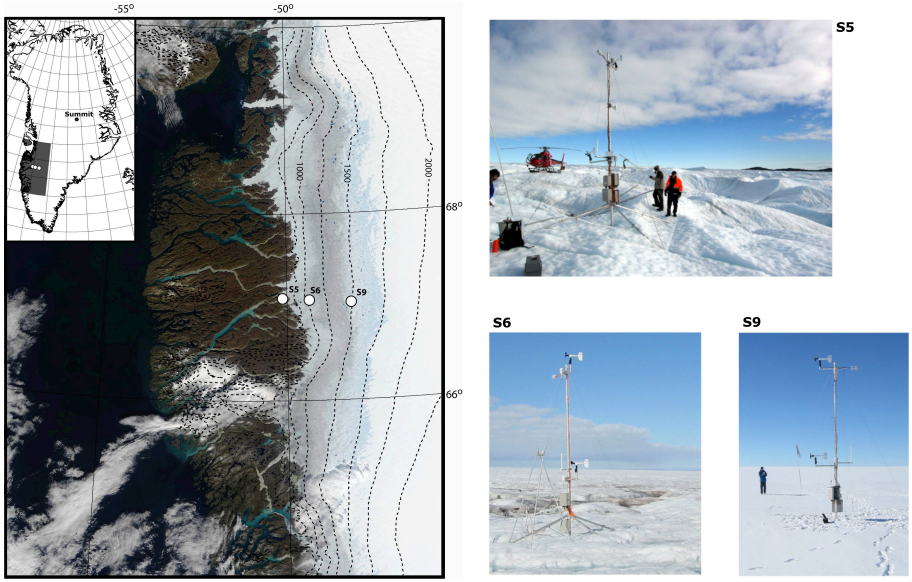

Fig. 1. Left: MODIS scene of west Greenland (23 August 2006) with AWS locations (white dots) and ice sheet elevation contours (dashed lines, height interval 250 m, from Bamber and others, 2001). Inset shows location of Summit. Right: Images of AWS locations at S5 (27 August 2006), S6 and S9 (both 26 August 2006).

TCD
5, 779–809, 2011

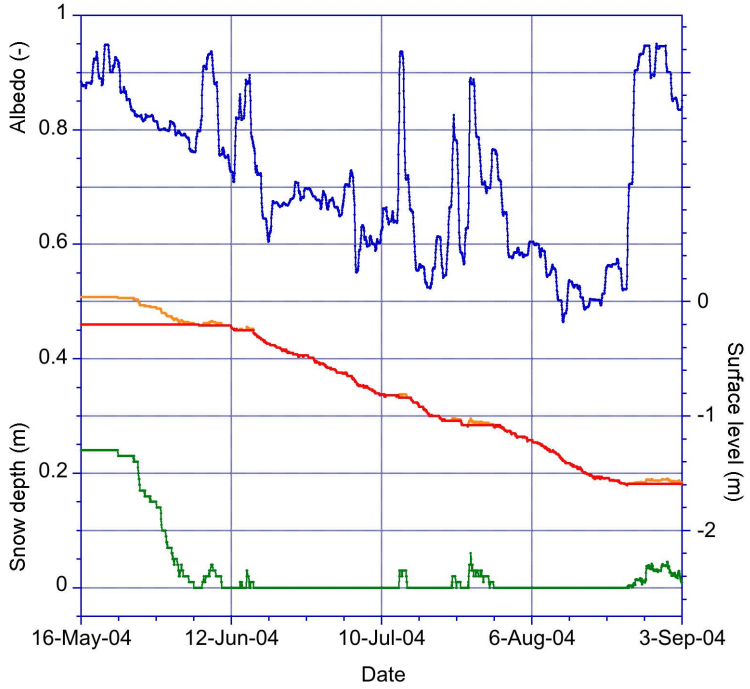

Fig. 2. Albedo (blue line, based on 24-hour running mean shortwave fluxes), snow surface (orange line), reconstructed ice horizon (red line) and associated snow depth (green line) derived from sonic height ranger measurements for S6, summer 2004.

TCD
5, 779–809, 2011

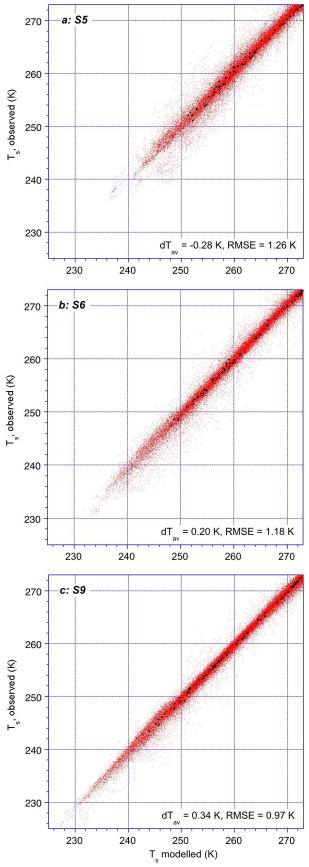

Fig. 3. Observed vs modelled surface temperature for hourly (red dots) and monthly averages (black dots) at S5 **(a)**, S6 **(b)** and S9 **(c)**. dT_{av} is average difference, RMSE is Root Mean Squared Error.

TCD
5, 779–809, 2011

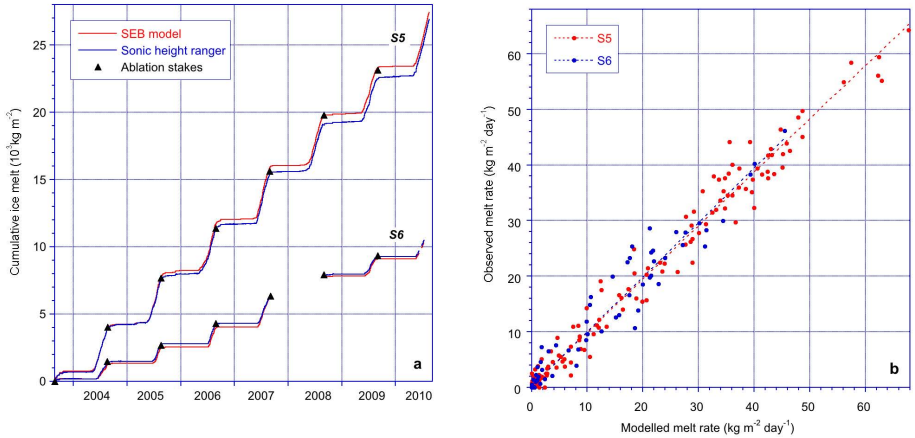

Fig. 4. (a) Observed (blue line) versus modelled (red line) cumulative ice ablation at S5 and S6. Cumulative ice melt from annual stake measurements are indicated by triangles. **(b)** Observed versus modelled 10-day average ice melt rates at S5 (red dots) and S6 (blue dots). The dashed lines are linear regressions on the data.

TCD
5, 779–809, 2011

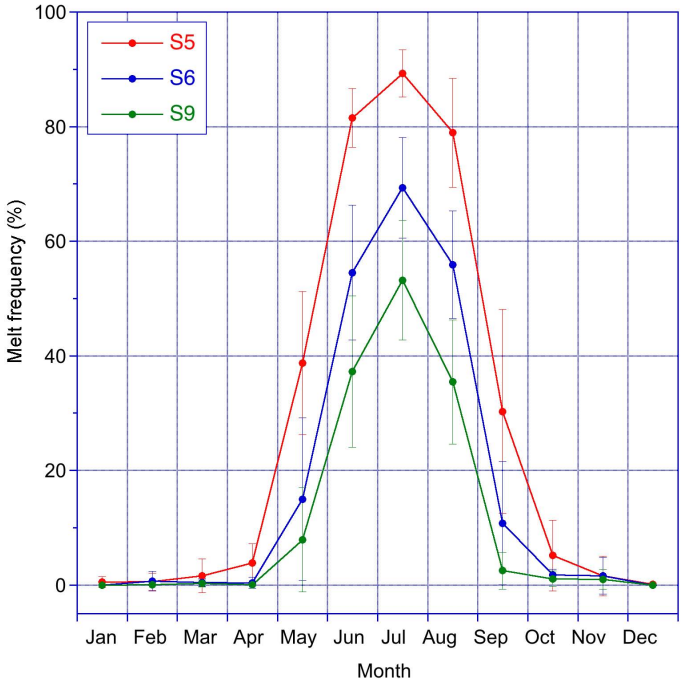

Fig. 5. Average seasonal cycle of melt frequency at S5 (red line), S6 (blue line) and S9 (green line). Error bars indicate standard deviation for the 7-year period.

TCD
5, 779–809, 2011

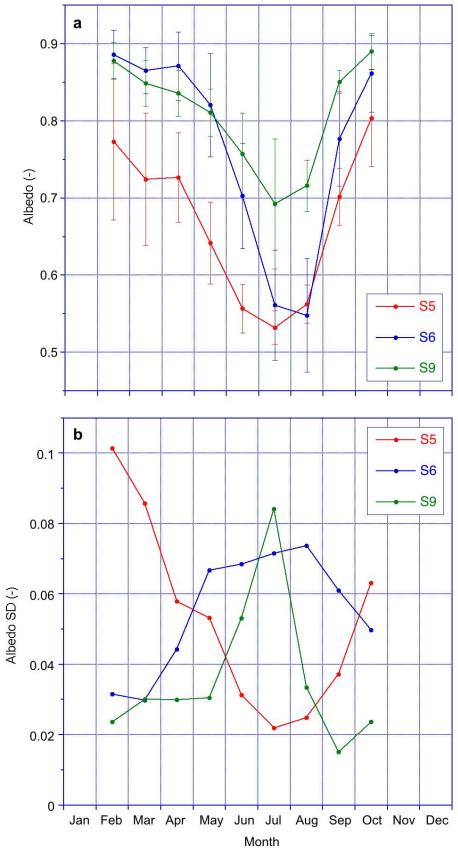

Fig. 6. Average seasonal cycle of albedo **(a)** (error bars indicate standard deviation for the 7-year period) and average seasonal cycle of the albedo standard deviation (SD) **(b)**.

TCD
5, 779–809, 2011

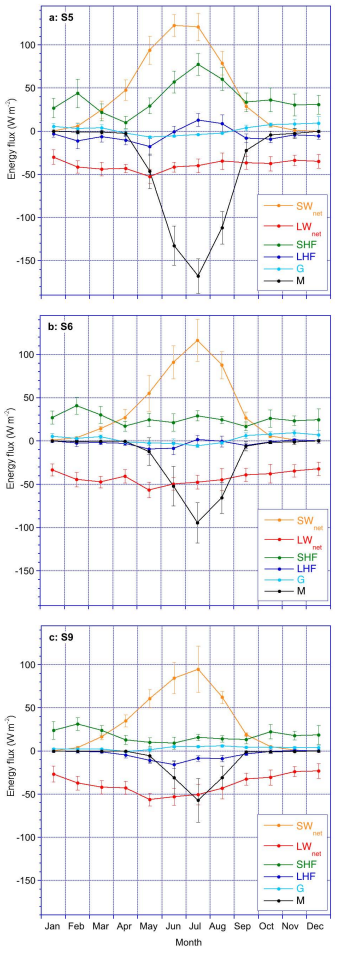

Fig. 7. Average seasonal cycle of SEB components at S5 **(a)**, S6 **(b)** and S9 **(c)**. Error bars indicate standard deviation for the 7-year period.

TCD
5, 779–809, 2011

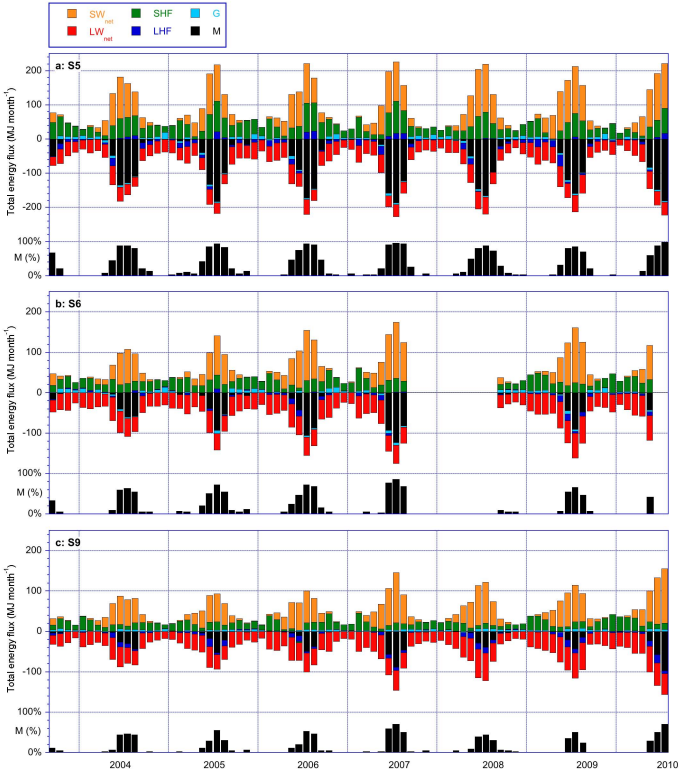

Fig. 8. Monthly mean SEB components and melt frequency (%) at S5 **(a)**, S6 **(b)** and S9 **(c)**.

TCD
5, 779–809, 2011

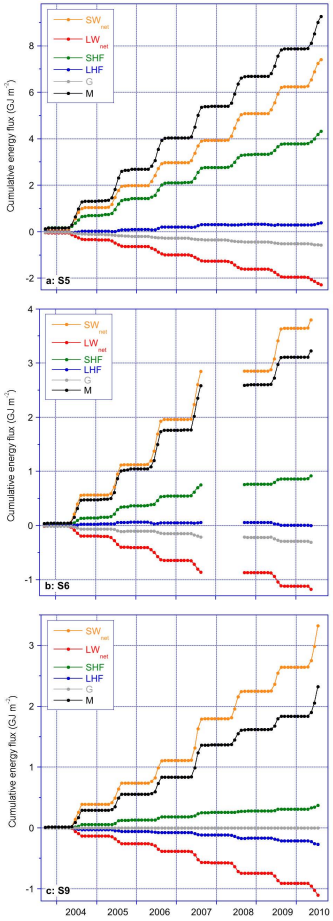

Fig. 9. Cumulative energy fluxes (10^3 MJ m^{-2}) during melt for S5 **(a)**, S6 **(b)** and S9 **(c)**.

TCD
5, 779–809, 2011

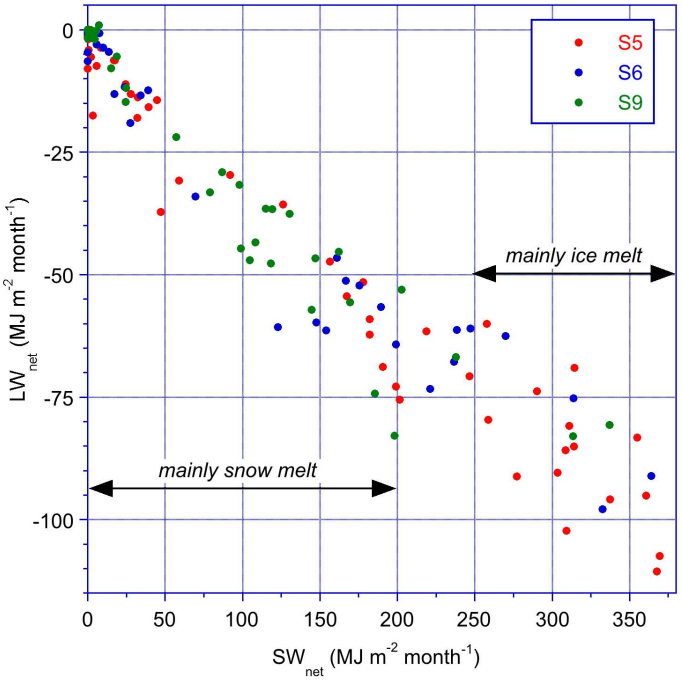

Fig. 10. Correlation of monthly mean net longwave and net shortwave radiation during melt for S5 (red dots), S6 (blue dots) and S9 (green dots).

TCD
5, 779–809, 2011

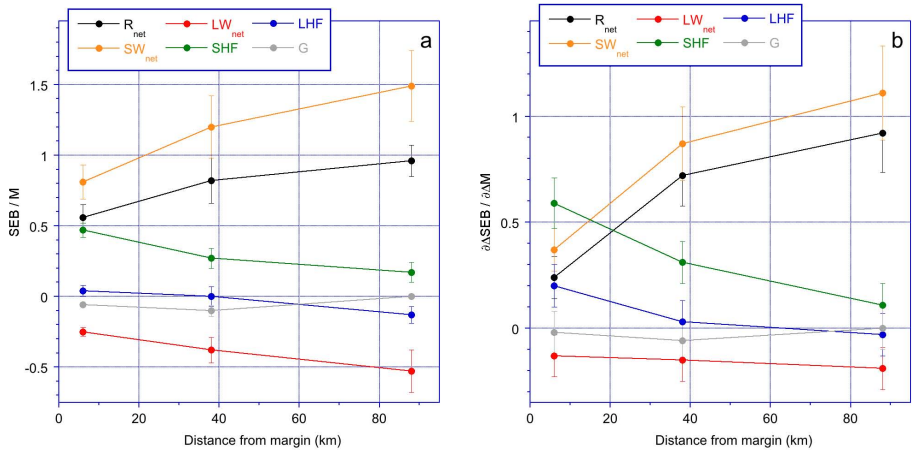

Fig. 11. Variation with distance from ice margin of **(a)**: fraction of total melt energy provided by SEB components (error bar indicate standard deviation from year to year) and **(b)**: regression slope of anomalies of cumulative monthly SEB energy components with anomalies of cumulative monthly melt (error bar represents standard deviation from regression performed on subsets of the data).

TCD
5, 779–809, 2011